Aerodynamic Performance of Morphing and Periodic Trailing-Edge Morphing Airfoils in Ground Effect

Dominic Clements[1] and Kamal Djidjeli, Ph.D.[2]

Abstract: Applying fish bone active camber morphing to the wing-in-ground effect to improve the aerodynamic efficiency was investigated using computational fluid dynamics (CFD) at a Reynolds number of 320,000. Steady-static morphing was first carried out with Reynolds-averaged Navier–Stokes (RANS) equations in two dimensions for morphing start locations off (60%, 80%, and 90% chord), ground clearances ($h/c = 0.1$, 0.2, 0.4, 1), and angles of attack (AoAs) 0°, 2°, 3°, 4°, and 12°. A morphing displacement (w_{te}) of 0.5% increased the efficiency by 2.8% (compared to non-morphing in the ground effect) for the 3° AoA and 90% start location, and by 62% in comparison to the baseline unmorphed airfoil in freestream. Reducing $h/c = 1$ to 0.1 increased the lift between 10% and 17%; the larger gain was with the highest morphing deflection. A key finding was that morphing the airfoil reduced the distance between the trailing edge and ground, enhancing the ground effect. Also, morphing at an earlier start location in the chord direction resulted in a smaller area beneath the airfoil, reducing the total pressure, which reduced the overall lift compared to a later morphing start location. Dynamic morphing at 1 Hz using URANS K-Omega-SST showed a similar amount of lift as static morphing but a slightly higher amount of drag. Reducing the period caused an initial overshoot in drag before settling. The dynamic ground effect showed higher efficiency at low AoAs compared to dynamic morphing in freestream, which is beneficial for aircraft to fly with less pitch. Finally, periodic morphing for $h/c = 0.1$ using sinusoidal motion with morphing starting at 25% along the chord and 4° AoA was investigated between 0.05% to 0.15% w_{te} and 0.5 to 3.5 Strouhal number. Periodically morphing at 0.125% w_{te} and Strouhal number of 0.9 using DES simulations increased the efficiency by 5.4%; however, it reduced the lift by 0.7%, the drag reduced by 5.8%, and it showed Kelvin–Helmholtz instability at 9.8 Strouhal number. **DOI: 10.1061/JAEEEZ.ASENG-4707.**

Practical Applications: The use of UAVs is increasing in popularity for many missions, which include observation, surveys (Narayanan and Ibe 2015), and the delivery of supplies, including medical. The use of UAVs typically has lower aircraft and operational costs as well as allowing the craft to carry out dangerous missions without putting the crew in danger. A wing-in-ground effect (WIG) craft typically operates on water due to the large fuel consumption savings as well as allowing the craft to travel at higher speed compared to conventional marine craft. The study focused on applying morphing wings to a UAV WIG effect craft to improve the aerodynamic performance of the craft and allow further fuel efficiency savings compared to a marine craft. The improved performance of the WIG craft and applying morphing translates to improvements in flight time and increased range. Morphing wings also allow the wing to adapt to different flight conditions allowing for optimized aerodynamic performance depending on factors such as cargo weight and weather conditions.

Author keywords: Computational fluid dynamics (CFD); Ground effect; Morphing wings; Dynamic and periodic morphing.

Introduction

Wings in proximity to the ground have been identified to enhance the performance of both wings and inverted wings. The performance of wing enhancement can be analyzed in two parts, chordwise and spanwise enhancement (Rozhdestvensky 2006). The spanwise performance gains are due to a reduction in induced drag and a reduction in the wing tip vortex strength. The chordwise enhancement is due to a dynamic air cushion under the wing increasing the pressure on the lower surface. A dynamic air cushion is formed due to the fixed trailing-edge pressure causing all the effects of the ground to occur upstream of the trailing edge. The channel between the lower surface and the ground acts as a venturi, increasing the pressure on the lower surface of the airfoil, increasing lift (Zhang et al. 2006).

The WIG effect is typically applied to marine craft/WIG craft to allow the craft to fly out of the water, reducing fuel consumption and increasing the speed and ride smoothness (Yun et al. 2010). Varying altitude dramatically affects the wing's lift, which increases at a greater rate closer to the ground. Typical ground effect clearances range in height below 50% of the chord. Below 10% is classified as extreme ground effect (Rozhdestvensky 2006), and 100% is considered freestream due to the unnoticeable performance gains at this height. The large variation in lift causes the airfoil moment to vary, which causes instability in pitch and roll, which is a drawback of WIG craft (Zarim et al. 2016).

Applying camber morphing to airfoils has been carried out in freestream for multiple applications, such as wing turbine blades (Wolff et al. 2014) and aircraft (Watkins and Bouferrouk 2022). The lift increased by deflecting the trailing edge (Xiang et al. 2019), and the wing can be optimized to provide optimum aerodynamic efficiency at different flight conditions (Abdessemed et al. 2017; Weaver-Rosen et al. 2020). Periodic morphing of trailing

[1]Ph.D. Student, Dept. of Computational Engineering and Design, Univ. of Southampton, Southampton SO16 7QF, UK (corresponding author). ORCID: https://orcid.org/0000-0003-4793-7733. Email: dc5g12@soton.ac.uk

[2]Dept. of Aeronautical and Astronautical Engineering, Univ. of Southampton, Boldrewood Campus, Southampton SO16 7QF, UK. Email: kkd@soton.ac.uk

Note. This manuscript was submitted on June 7, 2022; approved on December 12, 2022No Epub Date. Discussion period open until 0, 0; separate discussions must be submitted for individual papers. This paper is part of the *Journal of Aerospace Engineering*, © ASCE, ISSN 0893-1321.

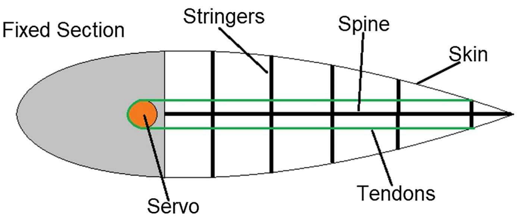

F1:1 **Fig. 1.** Fish bone active camber (FishBAC) concept.

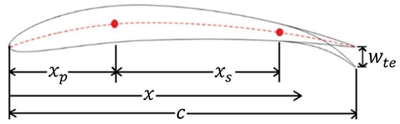

Fig. 2. Airfoil point location definition. F2:1

edges has been investigated (Kan et al. 2020) to delay the stall of wings in freestream, which has been found to delay stall by 2° using large trailing-edge displacements at low frequencies. For smaller trailing-edge displacements and higher morphing frequencies, it was seen that the aerodynamic performance could be increased at lower angles of attack (AoAs) using trailing-edge morphing in freestream (Abdessemed et al. 2021; Jodin et al. 2017).

Fish bone active camber (FishBAC) morphing is a method originally introduced by Woods and Friswell (2012), who defined a structure that allows airfoils to be morphed in the camber direction with a defined displacement. The method produces a bio-inspired structure that allows large camber deformations of the airfoil. Physical FishBAC airfoils specifically designed for UAVs consist of a beam with an airfoil profile defining stringers, and deformation is achieved using a rotational actuator operating a belt attached to the trailing edge, as shown in Fig. 1. The structure is then covered in a skin to form the airfoil profile surface.

In contrast to the numerous investigations of the rigid WIG effect, to the author's best knowledge, no research has been carried out yet on the aerodynamics of morphing WIG effect. This paper is arranged as follows. In section "Methodology," the morphing methodology is described. In section "Mesh Independence and Validation," a validation case is performed. Numerical simulations for ground effect morphing and dynamic and periodic morphing are discussed in section "Results and Discussion." Finally, conclusions were drawn in section "Conclusion."

Methodology

Computational fluid dynamics was used to investigate the aerodynamic flow around a NACA6409 airfoil in the ground effect. The NACA6409 airfoil was selected because it is a cambered airfoil having a greater volume beneath the airfoil and a substantial thickness for strength, which makes it practical for UAV applications. CFD was carried out in this study using Star CCM+, which is a multiphysics platform created in Java. The software was originally created by CD Adapco and sold to Siemens (Siemens 2016). Reynolds-averaged Navier–Stokes (RANS) equations are used with the k-omega SST turbulence model (Menter 1994) and revised k-omega (Wilcox 2008) within Star-CCM+, which provides improved predictions of flow separation under adverse pressure gradients. This strategy uses a second order upwind scheme for the spatial solution, a first order implicitly unsteady scheme for the unsteady simulations, and a segregated flow solver. The study was carried out at a Reynolds number of 320,000, with the chord as the characteristic length. This value was selected as it fell within the range for UAV craft (Lissaman 1983) and was above 100,000, where increasing the Reynolds number further has a minimal effect on the lift and drag (Winslow et al. 2018). The ground motion is simulated by applying a tangential velocity vector equal to freestream velocity to the ground boundary, which is assumed to be flat, rigid, and smooth. The inlet boundary is set to a velocity inlet, and the outlet to a pressure outlet. A control volume was used to limit the cell growth rate near the airfoil. Prism layers were used with 10 layers on the airfoil surface to capture the boundary layer with fixed height ensuring a $y^+ = 1$ throughout the mesh refinement.

Morphing of the airfoil was carried out by morphing the trailing edge at 60%, 80%, and 90% chord lengths from the trailing edge in the ground effect and freestream. The ground clearance was varied from $h/c = 0.1$, 0.2, 0.4, and 1, where c = chord length and h = clearance between the airfoil trailing edge and the ground. Four AoAs were tested (0°, 2°, 3°, and 4°) to compare the trailing-edge morphing length. Low AoAs were only tested, as a WIG effect craft usually produces a given amount of lift with an improved lift/drag ratio at lower AoAs. The study presents a static morphing airfoil independent of time using steady simulations. The airfoil geometry was morphed in MathWorks MATLAB code and imported into the CFD software.

The NACA6409 geometry used is parametrized and morphed in steady-static simulations. This method allows the airfoil to be dynamically morphed in future work. For a standard NACA airfoil, two equations define the curve of the camber line defined as y_c: the first equation (Eq. 1) defines the camber line from the leading edge to the point of maximum camber x_p, and the other defines the camber line from x_p up to the trailing edge. FishBAC morphing (Woods et al. 2014) adds a third equation to the camber line at a defined start location x_s. These three equations are shown in Eq. (2) and are used to define the entire camber line along the chord with morphing with a maximum chord thickness m and an airfoil chord c. The parameter ta defines the airfoil maximum thickness, and x an arbitrary location in the chord direction. In Fig. 2, the variable x_s defines the location from the leading edge to the start location along the chord where the FishBAC morphing begins. In this study, values of 60%, 80%, and 90% of the chord length were tested:

$$yt = 5t_a\left(0.2969\sqrt{\frac{x}{c}} - 0.126\left(\frac{x}{c}\right) - 0.351\left(\frac{x}{c}\right)^2 + 0.2843\left(\frac{x}{c}\right)^3 - 0.1015\left(\frac{x}{c}\right)^4\right) \tag{1}$$

$$y_c = \begin{cases} \dfrac{mx}{x_p^2}\left(2 * x_p - \dfrac{x}{c}\right), & 0 \le x < x_p \\ \dfrac{m}{(1-x_p^2)}(1 - 2x_p + 2x_p x - x^2), & x_p \le x < x_s \\ \dfrac{m}{(1-x_p^2)}(1 - 2x_p + 2x_p x - x^2) + \dfrac{w_{te}(x-x_s)^3}{(1-x_s)^3}, & x_s \le x \le c \end{cases} \tag{2}$$

For dynamic morphing, an implicit URANS solver was used to morph the airfoil using the FishBAC method with a time step of 0.001 s over 1 s morphing period corresponding to a Strouhal number of 0.002. This morphing frequency was selected with the mind of UAV craft that use low inertia moving parts and fast actuators widely available on the market for UAV craft. Remeshing was

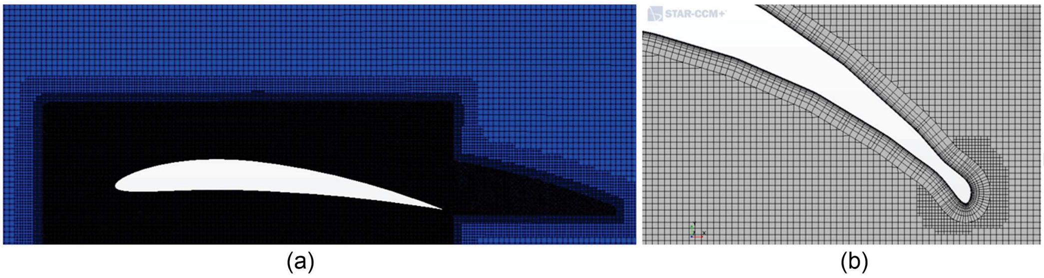

Fig. 3. (a) Mesh around NACA6409 airfoil; and (b) remeshed trailing edge.

carried out every 20 time steps to ensure the mesh quality remained high and the final mesh was valid for the mesh independence tests and validation. The remeshed trailing edge can be seen in Fig. 3. The trailing edge was a point at which the boundary layer cells were reduced using prism layer reduction within Star CCM+, which was also seen in a study by Ravindra (2018) investigating different types of mesh and the effect the mesh type had on the trailing edge.

This study also carried out periodic morphing using the FishBAC morphing method. Initially, the simulations were run using detached eddy simulation (DES) for 0.1 s with zero morphing to ensure a steady result. After 0.1 s, the morphing began initially deflecting a set displacement downwards, then upwards the same distance past the zero-deflection position. The morphing displacement for periodic morphing (y_{ts}) is carried out using a sinusoidal motion shown in Eq. (3), where f is the frequency of morphing, t is the instance in time, and w_{te} is the amplitude of deflection:

$$y_{ts} = w_{te} \cdot \sin(2\pi f t) \tag{3}$$

Due to the small deflections of 0.15% chord, the mesh quality remained high and, therefore, no remeshing was used for the periodic morphing. The simulation was initially run for 0.1 s with no morphing before the morphing was switched on; the simulation was then left to run for a total simulation time of 0.4 s. The results for the lift and drag were then averaged between the solution times of 0.15 and 0.4 s. Values for lift and drag were selected at 0.15 s; the solution settled, showing a converged mean lift and drag. A maximum time of 0.4 s was selected due to computational costs, which allowed 50 periods for a Strouhal number of 0.9 and 200 periods for a Strouhal number of 24 to be analyzed. Analyzing the results between 0.15 and 0.4 s was adequate due to small trailing-edge deflections of the 0.15% chord and high-frequency morphing of the Strouhal number between 0.5 and 3.5. This was also reported by Abdessemed et al. (2021), who noted that the amplitude of periodic morphing only varied by 0.3%. Computing the statics using the formulation of Parameswaran et al. (1979) for a Strouhal number of 0.9 resulted in a variance of 2.6×10^{-5} for the lift and 2.2×10^{-7} for the drag; the variance did not vary significantly when increasing the sample size to 24 for a Strouhal number of 3.5. The airfoil was held at 4° AoA and at 10% ground clearance to demonstrate periodic morphing in the ground effect. Due to computational costs, only the 4° AoA at 10% ground clearance airfoil configuration was tested for periodic morphing. Flying close to the ground at 10% shows large enhancements from the ground effect but is also a safe flying height, allowing the craft to roll and clear obstacles and rough terrain. Due to the vast number of variables, only a 4° AoA was selected due to computational costs; this study showed that this AoA had high aerodynamic efficiency.

Mesh Independence and Validation

To ensure the mesh and physics are adequate to capture the flow and provide consistent results, comparisons are made to existing data. A mesh convergence study was carried out, ensuring the mesh size was adequate to capture flow details and output consistent lift, drag, and moment coefficients for variations in mesh size. The mesh is varied by altering the mesh base size, which scales the far field and any areas of mesh refinement. The boundary layer mesh height was fixed to ensure that y^+ was equal to 1, as recommended in the software user manual (Siemens 2019) for the k-omega turbulence model.

A grid convergence study has been conducted using the ASME V & V 20 Committee (Coleman and Members 2009) to determine the discretization error. The lift and the drag coefficients for the NACA6409 at 0° AoA in Table 1 are computed using steady RANS and used for the evaluation of grid convergence. The coefficients are denoted by f, and the subscript denotes fine, medium, and coarse meshes.

The Richardson extrapolation using the two finest grids can be used to determine the zero-grid spacing value p for both lift and drag using Eq. (4), where the order of convergence is determined by the coefficient values of lift and drag defined by $p = \ln[(f_c - f_m)/(f - f_f)]/\ln(r)$. The grid refinement ratio is set to $r = 2$ as traditionally used (Coleman and Members 2009):

$$p_r = f_f + (f_f - f_c)/(r^p - 1) \tag{4}$$

A value of lift was calculated to be a Cl of 0.596 and a drag Cd of 0.0131 at zero grid spacing. The grid convergence index (GCI) is defined as Eq. (5), where F_s, a safety factor, is set to 1.25 for comparisons over three or more grids. The relative error ε defined as $\varepsilon = (f_f - f_m)/f_f$ for the fine mesh and $\varepsilon = (f_m - f_c)/f_m$ for the coarse mesh. A value of GCI = 0.114% for the fine and GCI = 0.723% for the coarse mesh was determined for the lift and a GCI = 0.0116% for the fine and a GCI of 0.572% for the coarse for the drag values:

$$GCI = \frac{F_s|\varepsilon|}{(r^p - 1)} \tag{5}$$

After determining the GCI, the solution needs to be checked using Eq. (6); it is within the asymptotic range of convergence.

Table 1. RANS mesh cell count with corresponding lift and drag values

Mesh refinement	Cell count	Cl	Cd
Fine	2,746,470	0.596	0.0131
Medium	724,877	0.599	0.0131
Coarse	148,704	0.618	0.0128

Table 2. RANS mesh size error

Mesh refinement	Cl error (%)	Cd error (%)
Fine	0.09	0.01
Medium	0.58	0.16
Coarse	3.58	2.69

Table 3. URANS mesh size error

Mesh refinement	Cl error (%)	Cd error (%)
Fine	0.46	0.01
Medium	1.53	0.30
Coarse	4.95	9.70

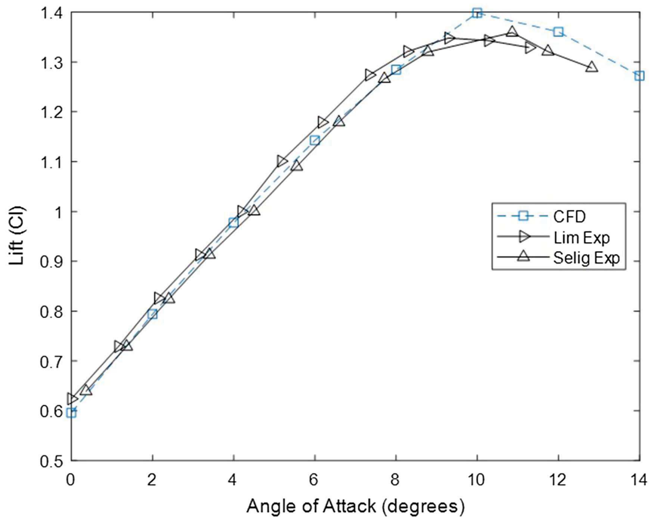

Fig. 4. CFD compared to experimental data.

Table 4. DES mesh size error

Mesh refinement	Cl error (%)	Cd error (%)
Fine	0.02	0.02
Medium	0.21	0.72
Coarse	2.66	27.07

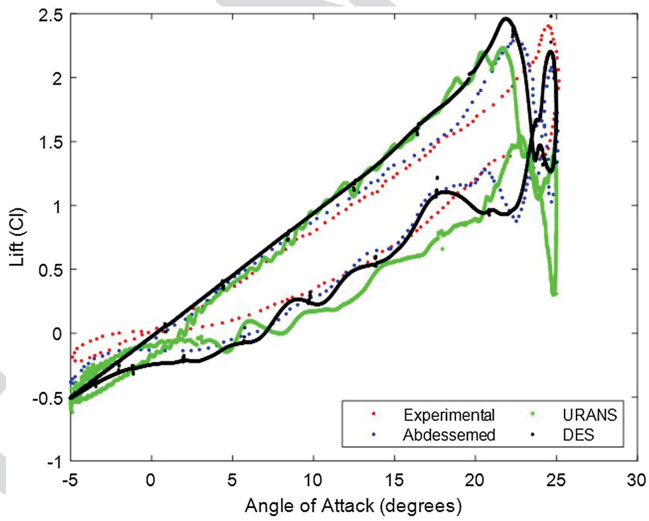

Fig. 5. NACA0012 pitching airfoil lift freestream.

This yields a value of 0.9951 for the lift and 0.9987 for the drag, which both are approximately 1 satisfying Eq. (6):

$$1 = \frac{GCI_{fm}}{(r^p GCI_{mc})} \tag{6}$$

Having checked the asymptotic range of convergence, the error for each grid refinement can be checked using the zero-grid value of lift and drag coefficients. From Table 2, the errors for both the fine mesh and medium mesh have converged to a small percentage. The medium mesh converged to within 0.58% for the lift and 0.16% for the drag and carried forward for the rest of the study, as using a fine mesh increases the computational costs with little gain in reducing the error.

Fig. 4 compares the CFD data of the NACA6409 in freestream to available experimental data (Lim et al. 2009; Selig et al. 1989) with similar Reynolds numbers. Below 10°, there is a strong correlation between the CFD and experimental data showing the validity of the CFD setup. At higher AoAs, the experiments predicted an earlier stall compared to the CFD. Overall, the CFD results are in good agreement with the experiment, so the validation of the CFD was accepted.

Further independence validation was carried out using unsteady Reynolds-averaged Navier–Stokes (URANS) and DES for dynamic morphing to ensure that the dynamic mesh and time step were valid. Independence was first carried out on a static airfoil for both URANS and DES at 4° AoA. The mesh size and time step were varied accordantly to keep the Courant number [Eq. (7)] equal to 1, as recommended by the CFD user manual (Siemens 2019):

$$CFL = u\frac{\Delta s}{\Delta x} \tag{7}$$

The corresponding mesh size and time step were then used, and three grid spacings were tested using the same method outlined in the RANS mesh independence using Eqs. (4) and (5) to determine the mesh independence for the URANS and DES simulations. The lift converged to 1.5%, and the drag converged to 0.3% at 1,200,000 cells for URANS in Table 3. For DES, the simulations converged to 0.21% for the lift and 0.72% for the drag at 500,000 in Table 4 compared to the zero-grid spacing solution.

Validation was carried out against experimental data of a pitching airfoil due to the lack of data for morphing a FishBAC airfoil in time. The NACA0012 airfoil was used for validation against the study carried out by Lee and Gerontakos (2004). The pitching motion was described by $\alpha_t = \alpha_m + \Delta\alpha \sin(\omega t)$, where $\alpha_m = 10°$ is the angle the airfoil pitches about, $\Delta\alpha = 15°$ is the pitching amplitude, t being time, and the pitching frequency $\omega = 2\pi f_o$, where f_o is the oscillation frequency. The reduced frequency described by $k = (\omega c/2U_\infty)$ was matched using a value of 0.1. The airfoil started at 10° and then increased to 25° AoA, where a strong trend between the CFD and experimental data was seen. A full pitching cycle was carried out before the lift plotted in Fig. 5, where a strong correlation was seen for the lift between 2° and 10°. Above 10°, the CFD began to show higher lift and an earlier peak at 22° for both the URANS and DES compared to the experimental data. The flow then stalled, reducing the lift before showing reattachment, causing a secondary lower magnitude peak at 24.5°. The flow in both the

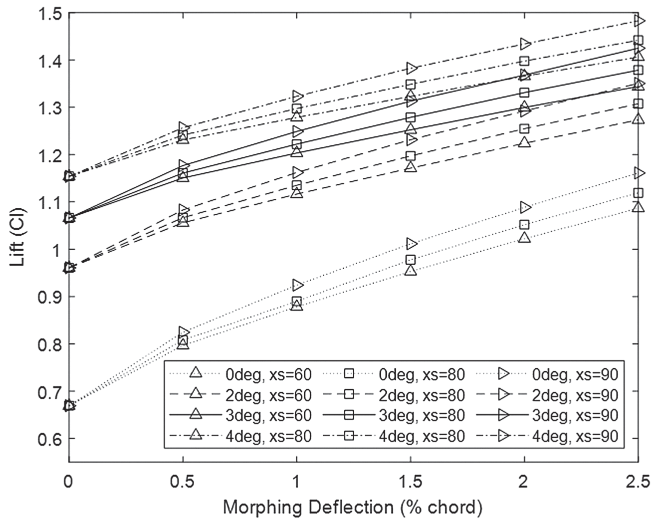

Fig. 6. Lift of NACA6409 for varying morphing start location ($xs = \%c$) at multiple angles of attack $h/c = 10\%$.

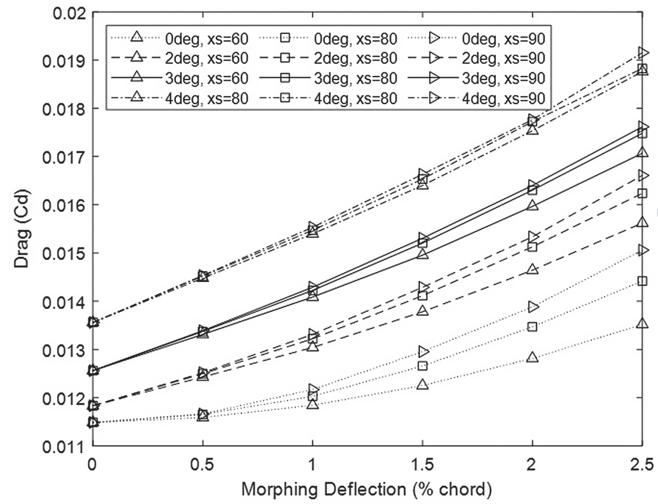

Fig. 7. Drag of NACA6409 for varying morphing start location ($xs = \%c$) angles of attack and $h/c = 10\%$.

experimental data and CFD struggled to reattach, causing a hysteresis loop where the lift was lower on the pitching-down stroke. As the pitching slowed down towards $-5°$ due to the nature of the sinusoidal motion, the flow had more time to reattach before pitching upwards, causing a greater lift on the upper surface. The lift was also compared to (Abdessemed et al. 2021). The URANS and DES simulation validations were accepted due to the high trend and similar lift coefficient values compared to the experimental data and the CFD case carried out by Abdessemed et al. (2021).

Results and Discussion

Effects of Morphing Trailing-Edge Deflection

The simulations were initially carried out at $h/c = 0.1$ ground clearance and different morphing trailing-edge deflection, morphing starting positions, and AoAs. Here, three distances for the start location of morphing were tested at the 60%, 80%, and 90% chord at AoAs of 0°, 2°, 3°, and 4°. (Figs. 6 and 7). As the trailing-edge morphing displacement increased, the lift (Fig. 6) and drag (Fig. 7) increased. The increase in lift is due to the variation in pressure on the airfoil's upper and lower surfaces. As the airfoil was morphed, it was seen (Fig. 8) that there was an increase in pressure on the lower surface and a suction increase on the upper surface, which increased the lift. The blockage effect on the lower surface from trailing-edge deflections caused mass flow reduction under the airfoil and forced the flow around the upper surface. The 0.5% and 2.5% deflected trailing edges have a single clockwise vortex at the trailing edge from the separated flow; the larger trailing-edge deflection shows two larger strength vortices (Fig. 9), like a Gurney flap. The suction peak on the upper surface increases (Fig. 8) at the airfoil's leading edge as the airfoil deflection increases, as seen by Moore et al. (2002), Ockfen and Matveev (2009), and Qu et al. (2014). For the drag, as the AoA increased from 0° to 4°, it was found that the drag increased, and it was highest for the 60% start location due to the flow separating earlier on the upper surface.

The effect of lift and drag can be combined by plotting the lift-to-drag ratio (Aerodynamic efficiency) versus the AoA, as shown in Fig. 10. It was seen from Fig. 10 that the most aerodynamically efficient trailing-edge distance was the 10% morphing at an

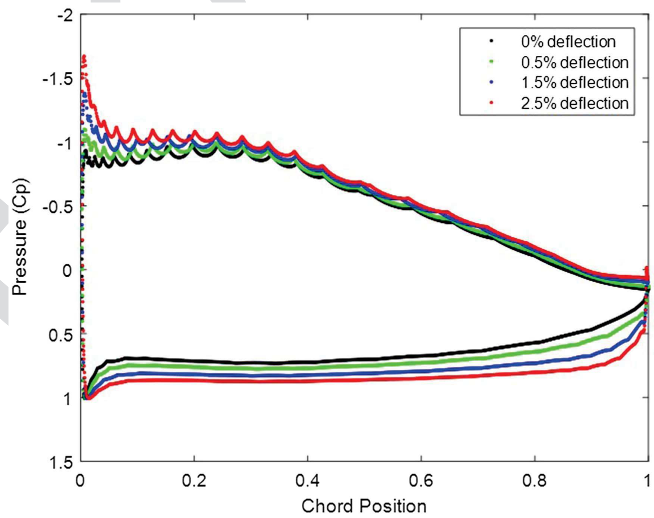

Fig. 8. Pressure distribution for morphing trailing-edge deflection at the 4° AoA, $xs = 80\%$, and $h/c = 10\%$.

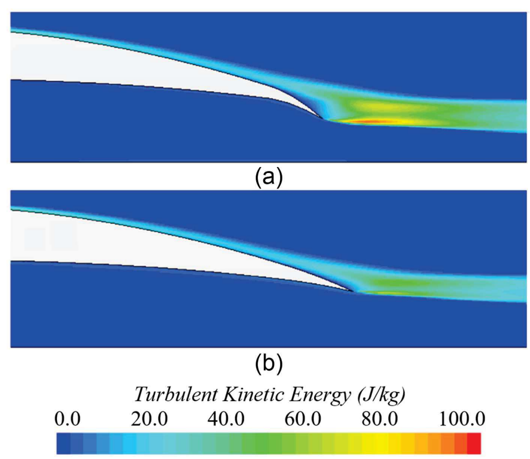

Fig. 9. NACA6409 TKE morphed (a) 2.5% and $xs = 90\%$; and (b) 0.5% in 10% ground effect and 4° AoA.

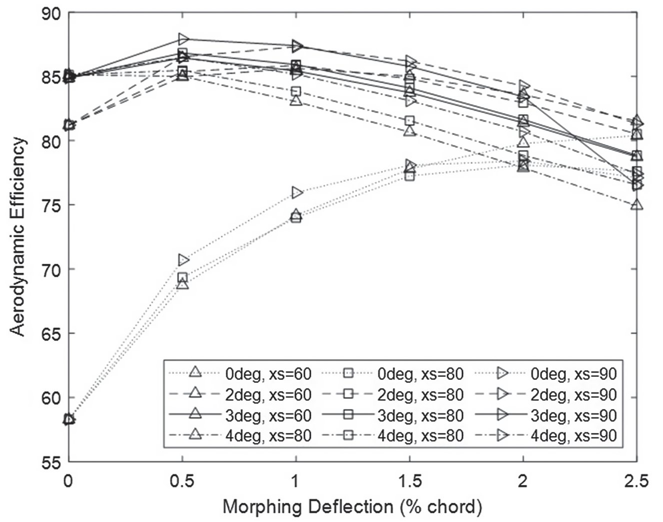

Fig. 10. Efficiency of NACA6409 for varying morphing start location ($xs = \%c$) multiple angles of attack $h/c = 10\%$.

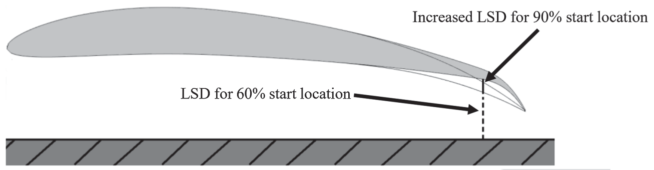

Fig. 11. Schematic of lower surface distance (LSD) for 60% and 90% start locations.

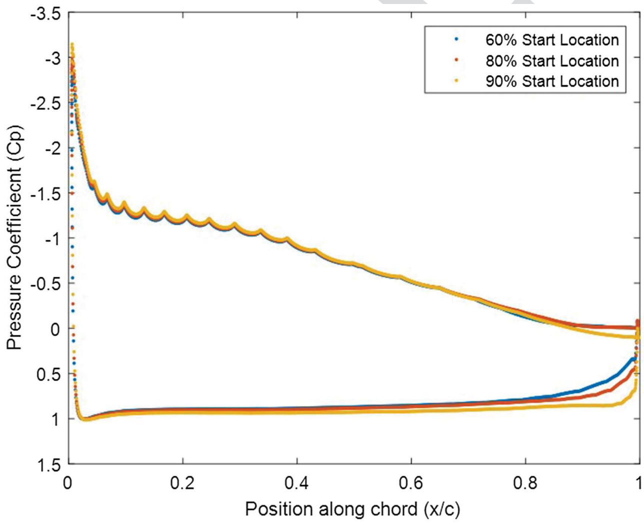

Fig. 12. Pressure distribution of 60%, 80%, and 90% start locations for 2.5% morphing distance at 4° AoA and $h/c = 10\%$.

AoA of 3° with an aerodynamic efficiency of 87.4. Comparing the nonmorphed airfoil in freestream to the morphed airfoil in the ground effect at the same AoA effect saw a 62% increase in aerodynamic efficiency. This increase in aerodynamic efficiency is obtained by averaging the lift and drag over the morphing period; the nonmorphed freestream aerodynamic efficiency is used as a baseline performance reference to see how much the morphed WIG effect increases the efficiency. As the airfoil was morphed, the drag increased of the airfoil, and all three morphing distances increased at almost the same gradient. (Fig. 7). Initially, the 60% airfoil had the least drag for small AoAs. For higher AoAs, the 60% airfoil flow began to separate earlier on the upper surface resulting in a slightly higher drag than the 90% and 80% distances (Fig. 7). The findings of morphing the airfoil in the ground effect are shown to agree with those of Ockfen and Matveev (2009), who tested an airfoil with a trailing-edge flap in the ground effect.

The lift for the morphing beginning at 90% from the trailing edge was the highest (Fig. 6) in all cases of the AoAs tested due to higher pressure on the lower surface for the 90% morphing airfoil seen in Fig. 11. It was seen that the pressure varied a significant amount on the morphed section [also seen in freestream for morphing wings by Abdessemed et al. (2018) and in ground effect on flaps by Ockfen and Matveev (2009)], which is where most gains in lift were seen for the later start location of 90%. The distance between the airfoil's lower surface to the ground and the distance between the trailing edge and the ground greatly impacted the ground effect enhancement. Due to the trailing-edge pressure being fixed by the Kutta condition, the trailing-edge pressure was the same for all morphing start locations (xs); therefore, varying the start location caused changes in pressure to occur upstream of the trailing edge. A later start location of 90% showed a greater distance between the ground and lower surface compared to the earlier start locations of 60% and 80%, which caused a high pressure on the morphed section shown in Fig. 11. This increased distance between the lower surface and ground increased the pressure (Fig. 12) on the morphed lower surface. Fig. 12 also shows a small increase of the suction peak on the leading edge for the 60% trailing-edge distance. The 10% morphing airfoil had the highest efficiency (Fig. 10) for all AoAs in the ground effect. Increasing the start location to high levels close to 100% chord shows that the morphed profile is like that of a Gurney flap. This is seen in Fig. 9, where two vortices behind the morphed section closely resembled those seen in Wang et al. (2008), which also explains the drop in suction on the trailing-edge upper surface for the 90% start location compared to 60% and 80%.

Comparing the velocity contours (Fig. 13) for the NACA6409 at 3° AoAs and $h/c = 10\%$ clearance shows similar velocity contours and wake size for the two trailing-edge morphing distances. The stagnation point moved slightly along the lower surface for the 90% morphing distance. The 90% start location also had a slightly faster flow over the upper surface, resulting in a slightly higher suction peak at the leading edge; this was also observed by Woods et al. (2014) for freestream conditions.

As the ground clearance is reduced, the lift (Fig. 14) increases due to the Kutta condition forcing all changes to occur upstream of the trailing edge. The channel between the airfoil and the ground acts as a venturi; with the fixed trailing edge, the pressure increases upstream of the trailing edge as the ground clearance is reduced. For each ground clearance, the trend was the same for lift (Fig. 14), drag (Fig. 15), and efficiency (Fig. 16).

When in the ground effect, there is little change to the suction surface pressure distribution from $h/c = 0.1$ to $h/c = 0.2$ (Fig. 17), but there is a significant change in pressure on the upper surface between the freestream and ground effect ($h/c = 1$ to $h/c = 0.2$). This is due to the ramming action of the flow under the airfoil in the ground effect, causing an increase in velocity on the upper surface, which was also seen by Nirooei (2018). Both the pressure on the suction and the pressure surface have increased when the airfoil has been brought into the ground effect. The upper surface pressure

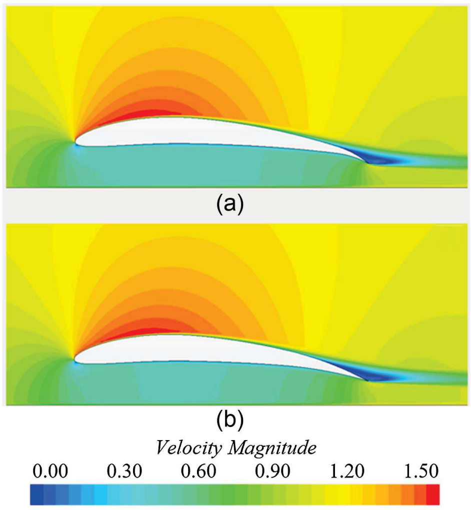

Fig. 13. Velocity contour of NACA6409 at (a) $xs = 90\%$; and (b) $xs = 60\%$ morphing start locations (nondimensional with freestream velocity).

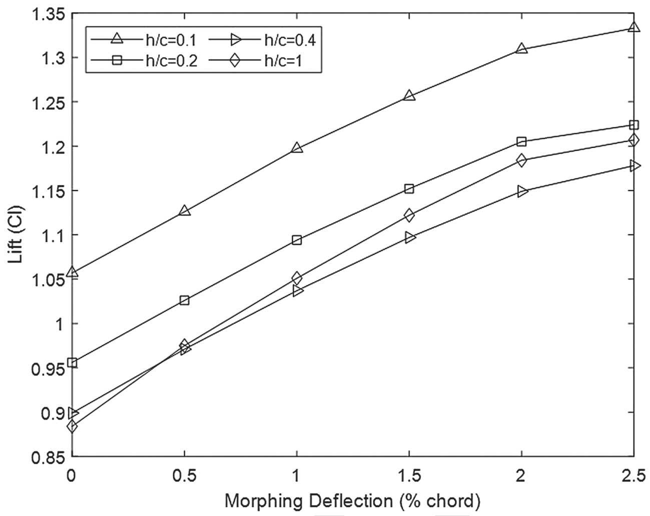

Fig. 14. Lift for 3° angle of attack NACA6409 morphed at ($h/c = 0.1$, 0.2, 0.4, 1) ground clearances and $xs = 60\%$.

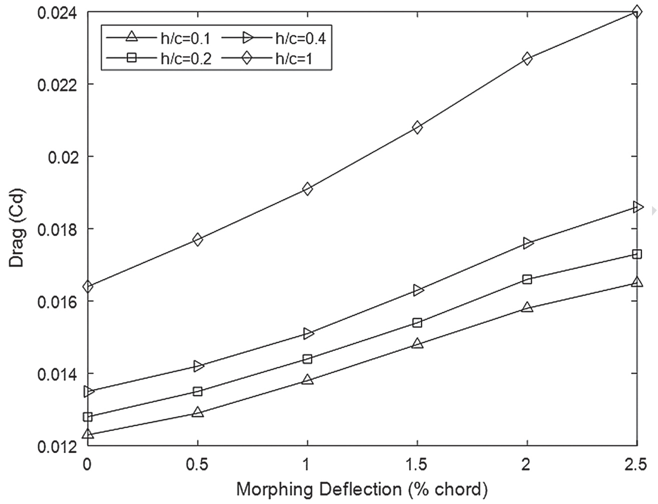

Fig. 15. Drag for 3° angle of attack NACA6409 morphed at ($h/c = 0.1$, 0.2, 0.4, 1) ground clearances and $xs = 60\%$.

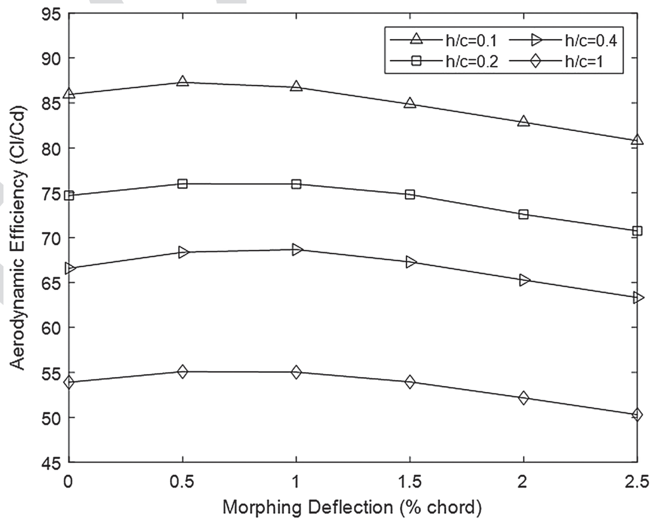

Fig. 16. Efficiency for 3° angle of attack NACA6409 morphed at ($h/c = 0.1$, 0.2, 0.4, 1) ground clearances and $xs = 60\%$.

increased due to the increased flow over the upper surface from the blockage under the airfoil, and the lower surface pressure increased due to the fixed trailing-edge condition that causes the effects of the ground to be felt upstream. Overall, the increase in pressure distribution is larger on the pressure surface (Fig. 17) compared to the suction surface, which gives an overall net increase in lift.

Bringing the wing from freestream to ground effect ($h/c = 1$ to $h/c = 0.4$), it was noted (Fig. 14) that the lift increased slightly; the lift increased a greater amount from $h/c = 0.4$ to $h/c = 0.2$ and increases the largest amount from $h/c = 0.2$ to $h/c = 0.1$. The drag (Fig. 15) decreased the largest amount from $h/c = 1$ to $h/c = 0.4$ and decreases the least from $h/c = 0.2$ to $h/c = 0.1$. The drag is reduced in ground effect due to the proximity of the ground reducing the downwash at the trailing edge of the airfoil. When the airfoil was in the ground effect, the downwash was reduced significantly compared to the freestream. Fig. 18 shows the streamlines for freestream, $h/c = 0.2$ and $h/c = 0.1$. For ground effect at $h/c = 0.1$ and $h/c = 0.2$, the streamlines are much more squashed together compared to the freestream reducing induced drag. Varying the height in ground effect from $h/c = 0.2$ to $h/c0.1$ shows the lowest change in drag as the flow is mostly parallel to the ground at $h/c = 0.2$. In the ground effect, the upwash of the incoming flow is turned upwards slightly at the leading edge. The stagnation point moved slightly downstream on the lower surface shown in Fig. 19 when in the ground effect.

The gains in lift varied when brought into the ground effect from freestream between 10% and 17%; the larger gain was with the highest morphing deflection. There was a reduction in drag when brought into the ground effect due to the proximity of the ground reducing the induced drag from the downwash. The flow separated earlier in the ground effect compared to the freestream due to the higher adverse pressure gradient on the upper surface in the ground effect and due to a reduction in downwash in close ground proximity.

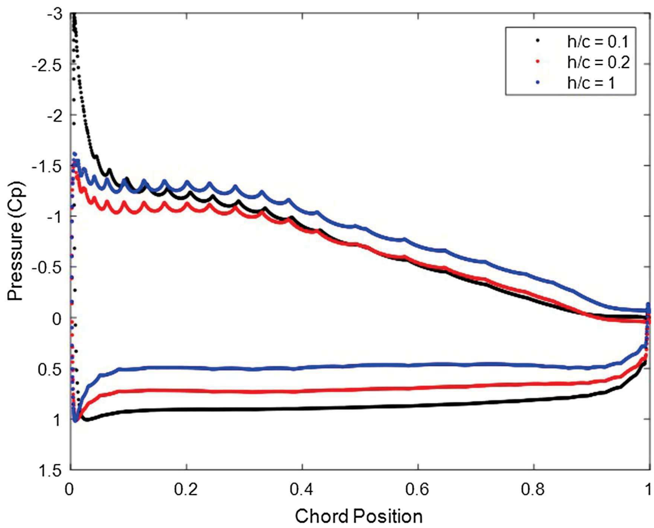

Fig. 17. Pressure distribution for varying height at 3° AoA.

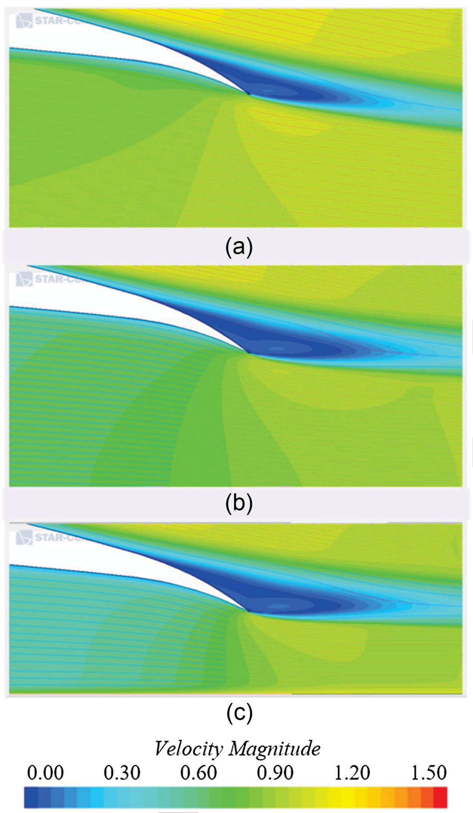

Fig. 18. Streamlines showing downwash for 2% deflection in (a) freestream; (b) $h/c = 0.2$; and (c) $h/c = 0.1$ (nondimensional with freestream velocity).

Although not focused on in this study, a brief look at the aerodynamic moment (3° AoA and $xs = 60$ configuration) in ground effect saw bringing the unmorphed wing from freestream with an aerodynamic moment of −0.158 to the ground effect with an aerodynamic moment of −0.128, which is a difference of 19%. Bringing the fully morphed 2.5% deflection wing from freestream with an aerodynamic moment of −0.196 to the ground effect with an aerodynamic moment of −0.222 showed a change of 11%. Also, morphing the airfoil from 0% to 2.5% in freestream caused an increase of the aerodynamic moment of 19% and in the ground effect of 35%. This showed that bringing a fully morphed wing from freestream to the ground effect caused a smaller change in aerodynamic moment. Morphing the WIG effect caused larger changes in aerodynamic moment compared to freestream, showing an increased pitch sensitivity for morphing WIG craft. This pitch sensitivity is extremely important, especially for WIG craft, so further investigation is required in future work.

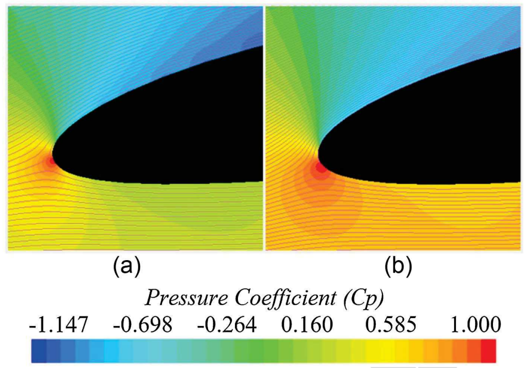

Fig. 19. Pressure contours and streamlines at (a) $h/c = 1$; and (b) $h/c = 0.1$.

Dynamic and Static Comparison

Morphing of the NACA6409 airfoil was carried out dynamically over a period of 1 s from 0% to 2.5% trailing-edge deflection. Morphing over 1 s was chosen due to UAV craft using fast actuators and low inertia, which allows morphing from zero to maximum deflection over short periods of time. The effect of reducing the morphing period was investigated for periods of 0.1, 0.5, and 1.5 s for the 4° NACA6409 airfoil at 10% ground effect. The morphing periods selected of 0.1, 0.5, 1, and 1.5 s correspond to Strouhal numbers of $2e^{-2}$, $4e^{-3}$, $2e^{-3}$, and $1.3e^{-3}$, respectively, which show the flow is quasi-static. The morphing was run over the defined period for an extra amount of time for the flow to settle. It was seen Figs. 20 and 21 that, changing the morphing period, the final lift and drag coefficients were identical for all morphing periods. For the drag only, it was seen for the 0.05 s morphing period that the drag overshot the final steady drag. The drag increased to a Cd of 0.0196 at 0.1 s before reducing to 0.0176, which was an overshoot of 10.8%. For the 0.1 s morphing, the drag was overshot by 5.4%, 1.2%, for the 0.5 s morphing and the 1 and 1.5 s drag did not overshoot the final steady-state value. The reason the drag overshot was that the rapid morphing caused higher levels of unsteadiness and increased separation of the morphed section of the airfoil, which over time became reattached to the airfoil. The slower morphing allowed the flow to remain attached throughout the morphing period. This overshoot in drag but not in lift was also seen in Abdessemed et al. (2019, 2022), in which a higher overshoot was observed for high morphing frequencies.

Using a morphing period of 1 s, the pressure around the airfoils was investigated for the 3° and 8° AoAs (Fig. 22). Analyzing the pressure as the airfoil was morphed over time showed (Fig. 22) the pressure increased upstream of the trailing edge as the airfoil was morphed, which this increase in pressure increased the lift of the airfoil, also seen in the static case. For both the 3° and 8° AoAs, there is a slight increase in pressure on the upper surface at the

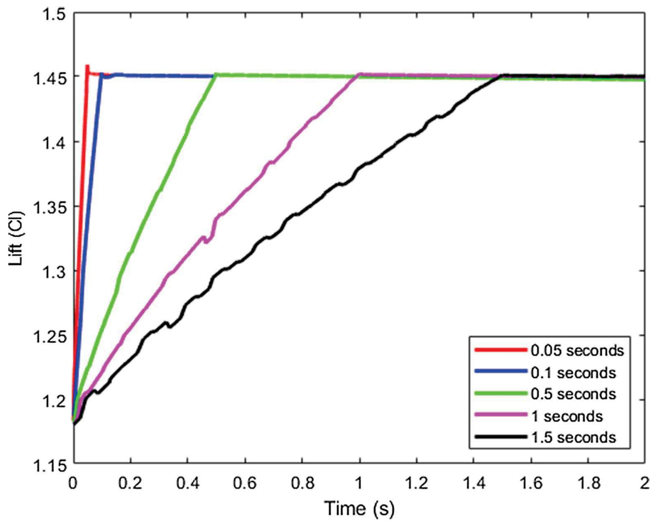

Fig. 20. NACA6409 lift varying morphing period.

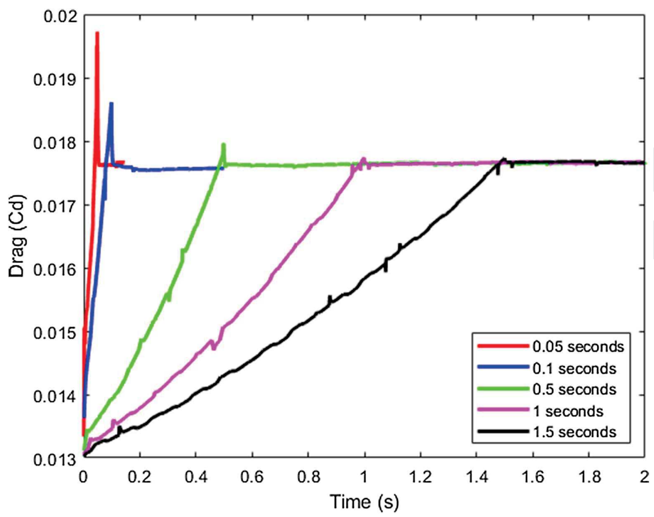

Fig. 21. NACA6409 drag varying morphing period.

leading edge, but most of the gains in the lift are on the lower surface. For the 8° AoA, the pressure beneath the airfoil was much larger than for the 3° AoA. For both cases, it was seen as the airfoil was morphed dynamically that the pressure increased upstream of the trailing edge, also seen for the static case shown in Fig. 12. Due to being quasi-static, the dynamic and static morphing showed very similar results at low AoAs.

Comparing the pressure coefficient for the static and dynamic cases (Fig. 24) at 8° in 10% ground effect showed little variation between the two cases due to the morphing Strouhal number being low, implying quasi-static flow. The effect of little variation in the pressure (Fig. 24) around the airfoil resulted in little variation in lift (Fig. 23). For the dynamic case, the lift was, on average, 1% higher than the static case for the 6° AoA and 3% higher than the static case at the 0° AoA. This showed that the effect of morphing over time compared to steady-state simulations had a minimal effect on the lift. This can be seen in Fig. 22 comparing the pressure coefficient around the airfoil. The pressures around the airfoil are almost identical for dynamic morphing and static morphing, therefore generating similar levels of lift (Fig. 24).

Direct comparison of the static and dynamic drag values was made for the corresponding trailing-edge deflection shown in Fig. 25. The drag is an average of 8% higher for the static case compared to the dynamic at 6° AoA and is 3% higher at 0° AoA. Analyzing the turbulent kinetic energy (Fig. 26) around the airfoil shows higher amounts of TKE around and downstream of the leading edge on both the upper and lower surfaces for the static case. The reason the drag was higher in the static case compared to the dynamic was that the dynamic case using URANS captured a greater amount of mixing, which reduced the amount of separation on the upper surface. As a result of the higher drag for the static morphing, the efficiency is an average of 4% lower for the dynamic morphing across the entire displacement at a 0° AoA and an average of 8% lower at a 6° AoA, as shown in Fig. 27.

Dynamic Behavior at High Angles of Attack

The stall and wake behavior was investigated using URANS dynamically between 8° and 16° AoAs in 2° increments in the freestream and ground effect of 10% ground clearance. In freestream at the 8°, 10°, and 12° AoAs, the lift (Fig. 28) increased as the airfoil was morphed. After the maximum morphed deflection of 2.5% chord was reached after a period of 1 s, the lift remained steady. It was seen that the 12° AoA was initially a higher lift value than the 10° AoA. At 0.5 s during the morphing, the lift of the 12° AoA intercepted the 10° AoA and had an overall lower final lift value after morphing. This was due to the airfoil approaching stall and showed the morphed airfoil had a lower stall AoA compared to the unmorphed. As the AoA was increased, the delta lift from zero to full deflection decreased. The gain in lift for the 8° AoA was a Cl of 0.264; at 10°, the gain was 0.233; and at 12°, the gain was 0.155.

The 12° AoA showed that when the airfoil was fully morphed, that stall was approached. Increasing the AoA caused stall to occur at zero morphing deflection, and increasing morphing resulted in a minimal gain in lift. For 14° at 0.8 s, as the morphing period of 1 s was approached, the lift became slightly unsteady. At 16°, the lift was highly unsteady throughout the morphing showing the flow had fully stalled and detached. The average maximum lift (Fig. 28) at 8°, 10°, and 12° was similar, showing trailing-edge stall was occurring as the lift did not abruptly reduce once the maximum lift was reached. The turbulent kinetic energy (Fig. 29) for 16° AOA showed a vortex-shedding structure similar to that in Abdessemed et al. (2018), with the shedding occurring at a Strouhal number of 20.5, which explains the sudden reduction and unsteadiness in lift and drag values. At a location 150% chord downstream of the trailing edge, the nondimensional vertical velocity compared to freestream is seen at 2 s, showing the presence of the vortex (Fig. 29). A separation bubble on the trailing edge grows to cover the upper surface, then suddenly bursts, causing the shedding as the upper surface tries to reattach, then bursts again. Fig. 29 shows the TKE at 12°; there is some slight oscillation in the wake, which explains the slight variations in lift and drag. Increasing the AoA to 16° shows (Fig. 29) the wake being highly unsteady with vortex shedding. The results of dynamic morphing with an oscillating wake were also observed by Abdessemed et al. (2018). For the 12° AoA in freestream, there was no dominant frequency, whereas increasing the AoA to 14° shows a small amplitude at a Strouhal number of 22.5, where the wake was showing unsteadiness from the shear layers interacting at the trailing edge from the unsteadiness of the separated flow on the upper surface (Jodin et al. 2017). Increasing the AoA further increased the magnitude of the spectra analysis, but shedding occurred at a Strouhal number of 20.5, and

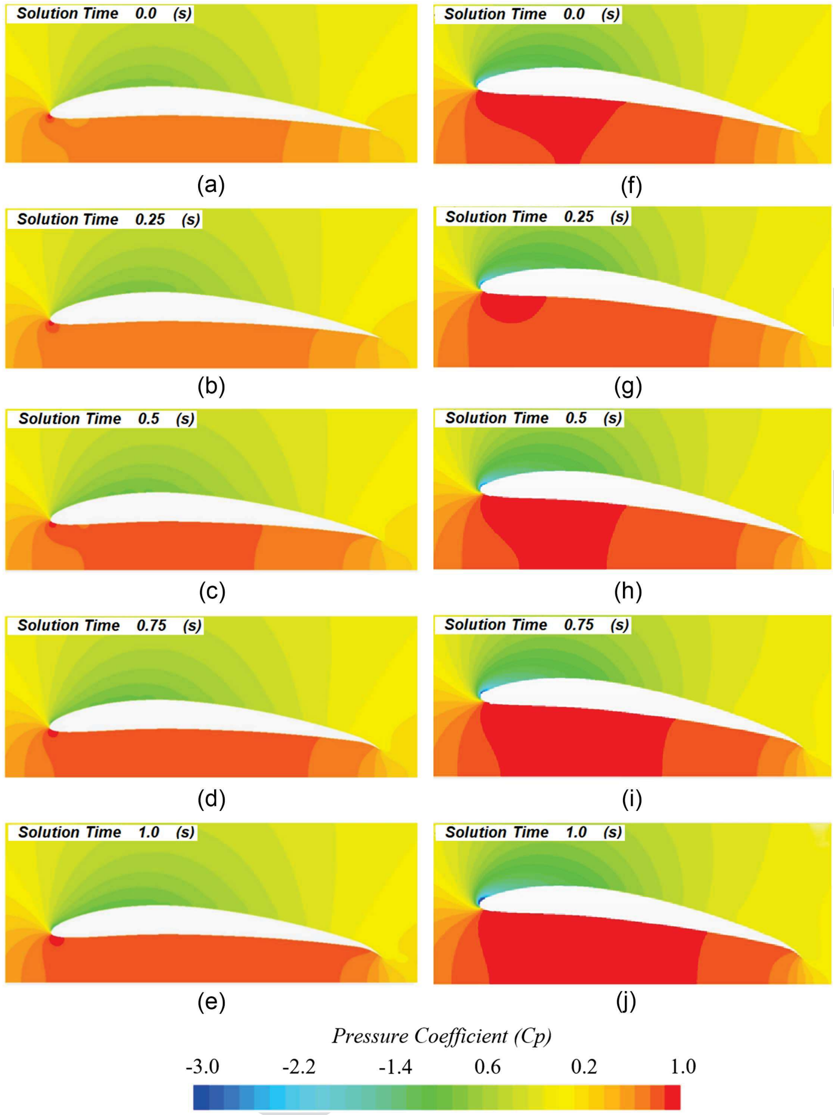

Fig. 22. Dynamic morphing of NACA6409 airfoil at (a)–(e) 3°; and (f)–(j) 8° angle of attack, $h/c = 0.1$ ground clearance, and $xs = 90\%$.

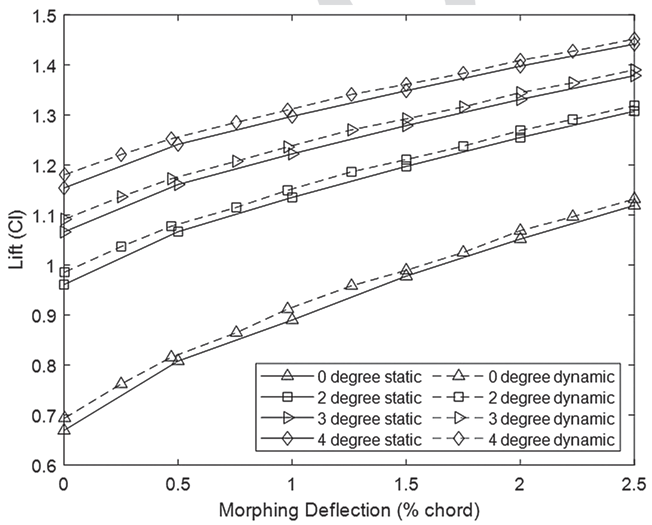

Fig. 23. Dynamic morphing lift at low AOA in 10% ground clearance and $xs = 80\%$.

from the size of the peak, sheading was seen to occur (Thakor et al. 2020). The vertical velocity component was shown in Fig. 30 at a location 150% downstream of the trailing edge, showing the vortex downstream.

In 10% ground, morphing the airfoil dynamically at high AoAs has been shown to reduce the oscillations of the wake seen by the lift (Fig. 31) and drag (Fig. 32). At 8°, the flow was found to have a small amount of separation on the suction surface, but the flow remained attached. Starting at zero morphing, the 10° AoA had a larger lift, but as morphing was increased, the flow began to stall at 0.3 s. At 0.83 s, the flow showed highly oscillating behavior; this was due to the airfoil being on the verge of fully separated flow, and the flow kept reattaching and detaching. Morphing the airfoil has shown the airfoil will stall at lower angle AoA as the airfoil curvature increases. As the airfoil is morphed in the ground effect, the AoA where stall occurs was at 10° compared to freestream at 12° showing the airfoil stalled at lower AoAs when in the ground effect. This means the wing operates more efficiently at lower AoAs. This is beneficial for aircraft since the setting angle for the wing can be smaller, or the UAV/plane can fly with less pitch, reducing drag and increasing flight efficiency. After 10° in the ground effect, the initial

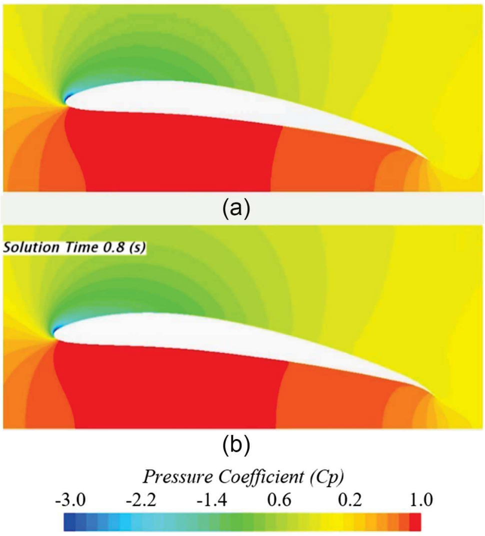

Fig. 24. Pressure plots of (a) statically morphed; and (b) dynamically morphed NACA6409 airfoil at $h/c = 0.1$ ground effect and 8° angle of attack.

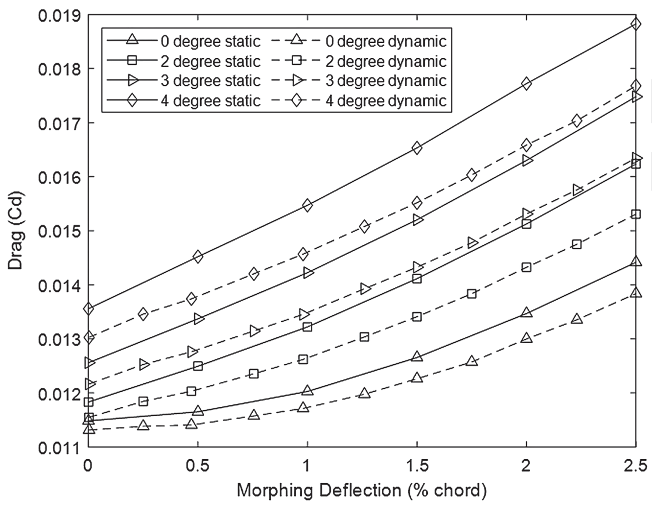

Fig. 25. Dynamic morphing drag at low AOA in 10% ground clearance and $xs = 80\%$.

start value of lift was much lower for 14°. Morphing the airfoil dynamically with a stalled upper surface showed the lift increased due to the flow being attached to the lower surface, and reducing the clearance between the trailing edge and ground caused an increase in pressure on the lower surface. Increasing the AoA to 16° initially showed the same lift as the 10° AoA due to the upper surface being stalled. As the distance between the trailing edge and ground reduced while morphing, the lift increased as the pressure on the lower surface increased. Compared to freestream, where vortex shedding was seen at a Strouhal number of 20.5, at 16° in the ground effect, there was no vortex shedding as the flow remained fully detached due to the proximity of the ground reducing downward momentum. At 10°, where oscillations in lift were seen (Figs. 31 and 32), a peak occurred in the spectra at a Strouhal number of 32; therefore, it is seen that for airfoils at high AoAs, introducing the proximity of the ground eliminated the vortex shedding.

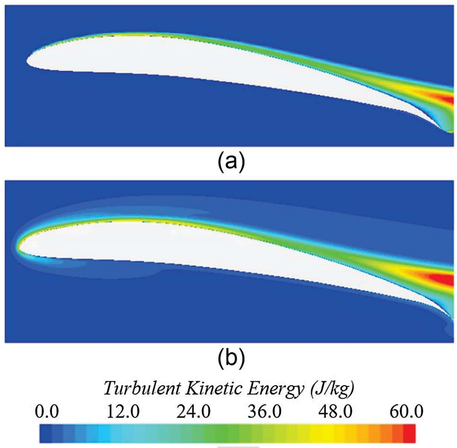

Fig. 26. Turbulent kinetic energy of NACA6409 airfoil at $h/c = 0.1$, 8° angle of attack, and 2.5% morphed deflection and $xs = 90\%$ for (a) dynamic; and (b) static.

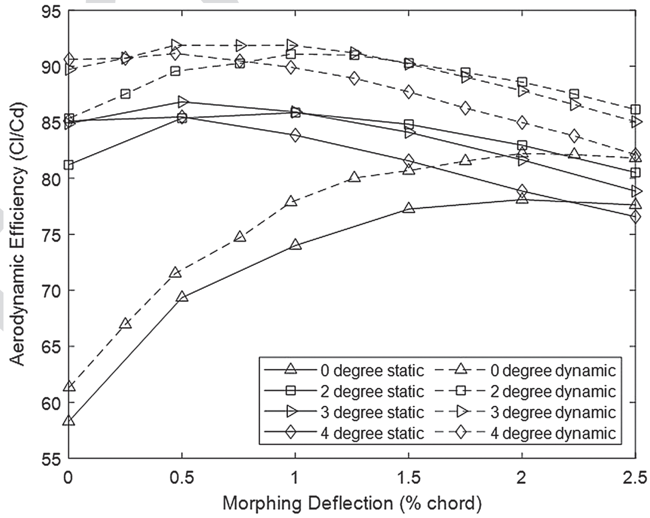

Fig. 27. Dynamic morphing efficiency at low AOA in 10% ground clearance and $xs = 80\%$.

As the AoA increased, the drag (Fig. 32) increased; increasing the morphing deflection also increased the drag. This was also seen for the airfoil in freestream (Fig. 33); however, the drag coefficient oscillated at high levels for the freestream case. As the drag increased for increasing the morphing deflection and AoA, the efficiency was shown (Fig. 34) to decrease. This was contrary to lower AoAs, where the efficiency initially increased before decreasing. The decreasing efficiency showed that the rate of drag increase was much higher than the rate of lift increase.

Due to the proximity of the ground, the wake was bounded by the ground and did not oscillate compared to the freestream; therefore, the lift and drag showed greater steadiness in the ground effect. The proximity of the ground was found to reduce the vortex shedding behavior shown in the TKE plots (Fig. 35) comparing the NACA6409 at the 16° AoA in both the freestream and ground effect. Moreover, using dynamic transient simulations reveals that the morphing motion has less influence on the local flow fields in the ground effect for high AoAs in comparison to those in the freestream.

At low AoAs, comparing freestream to ground effect shows (Fig. 36) that throughout morphing the ground effect had high aerodynamic efficiency. Comparing the freestream to the ground effect for the 8° AoA (Fig. 36) showed that the airfoil in the ground effect initially had a lower efficiency. Although an airfoil will create its maximum lift with some separation on the upper surface, the 8° in the ground effect had higher levels of separation on the upper surface, which increased the drag, causing a lower aerodynamic efficiency. Morphing the airfoil over time caused the 8° ground effect

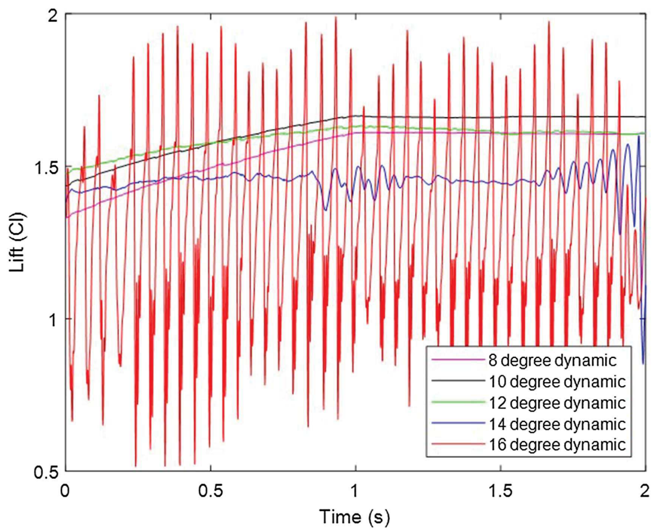

Fig. 28. Lift of NACA6409 in freestream morphed dynamically between 8° and 16° AoAs.

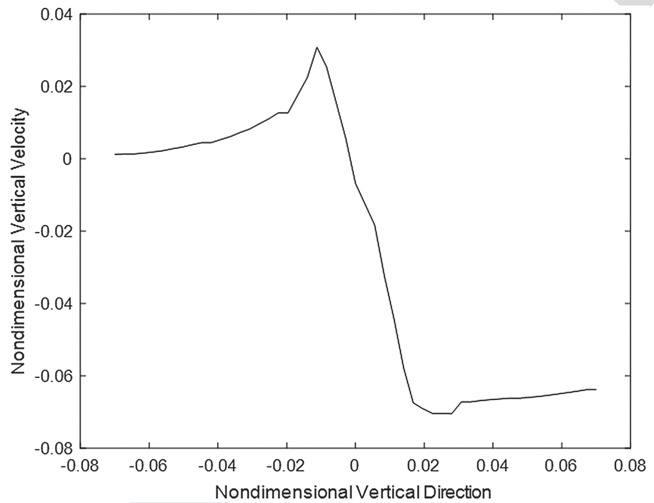

Fig. 30. Nondimensional vertical velocity in wake at 150% downstream of the trailing edge for 16° AoA in freestream.

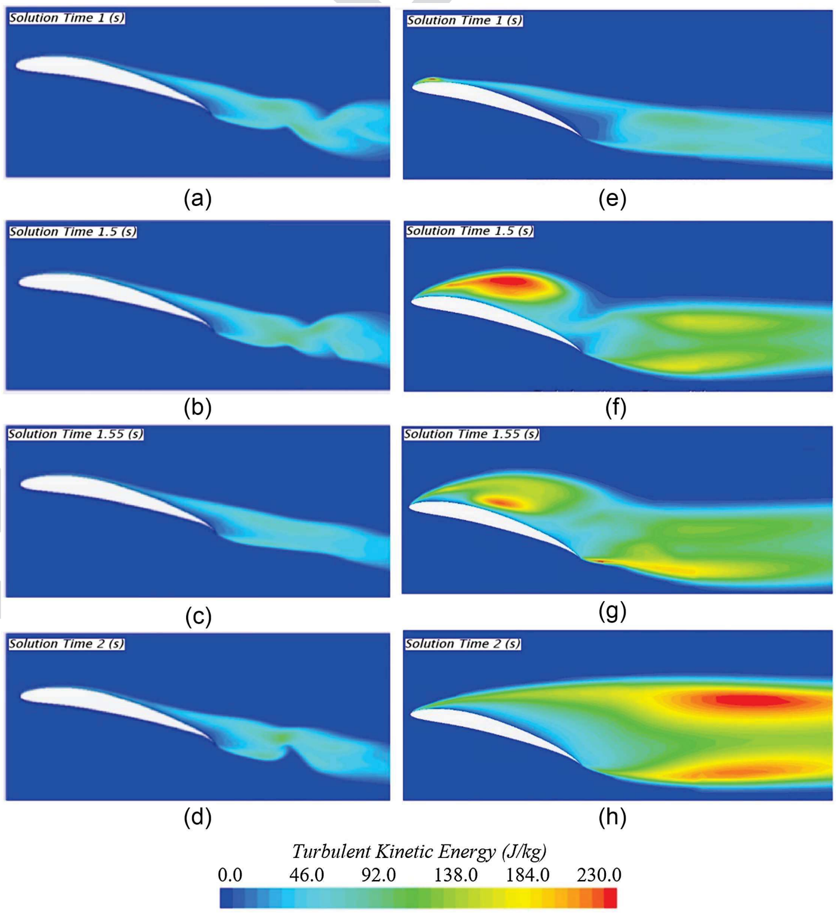

Fig. 29. Dynamic freestream (a)–(d) 12° AoA; and (e)–(h) 16° NACA6409 TKE.

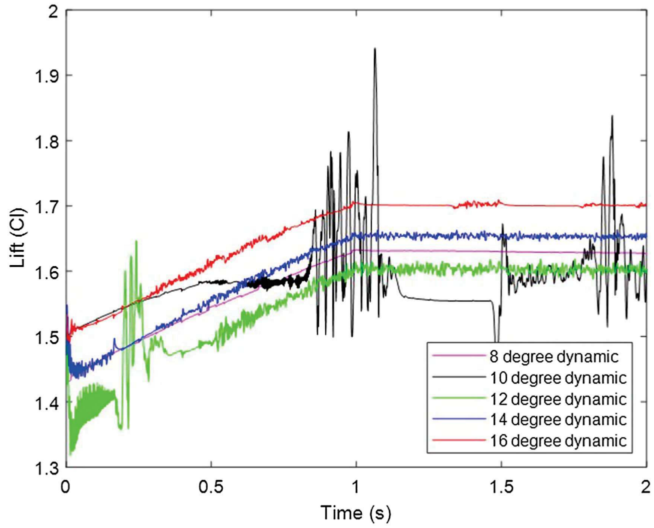

Fig. 31. Dynamic morphing lift with ground clearance $h/c = 0.1$, $xs = 80$.

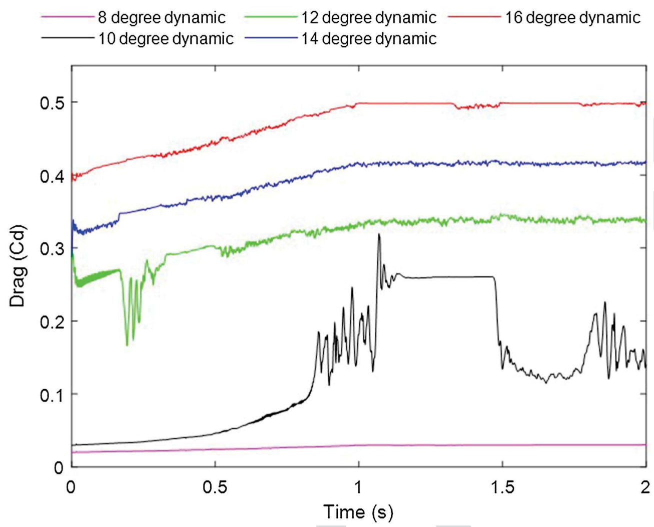

Fig. 32. Dynamic morphing drag with ground clearance $h/c = 0.1$.

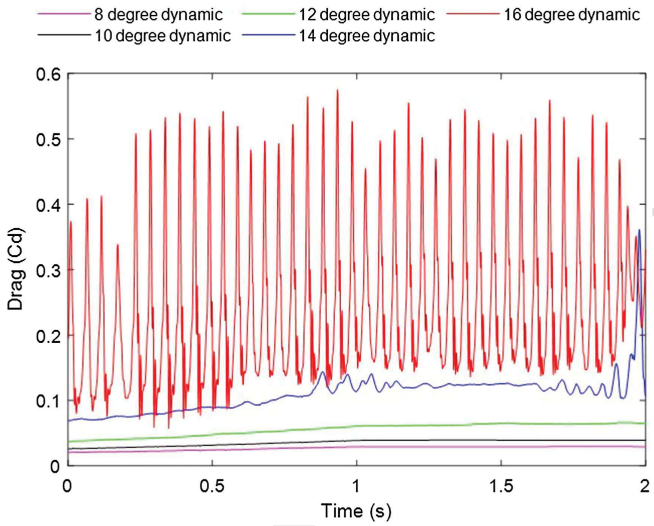

Fig. 33. NACA6409 drag in freestream morphed dynamically between 8° and 16° AoAs.

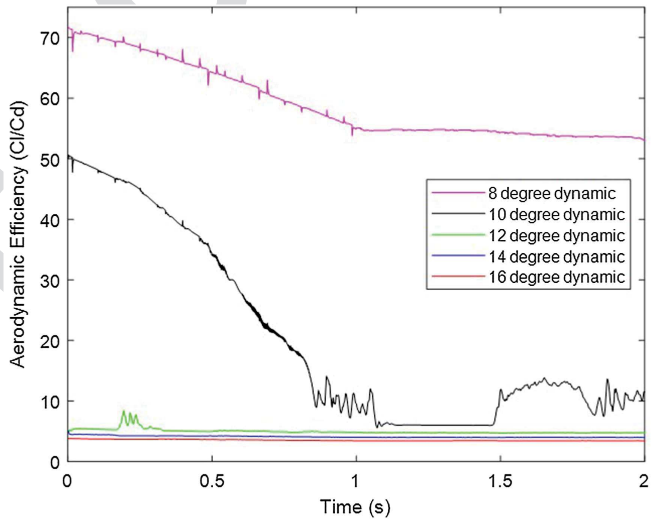

Fig. 34. Dynamic morphing efficiency with ground clearance $h/c = 0.1$.

airfoil to have a higher aerodynamic efficiency due to the greater increase in lift from being in the ground effect as the airfoil was morphed. This was opposite to the lower AoA ground effect, where the ground effect efficiency was much higher than the freestream case throughout the morphing shown by the 3° AoA (Fig. 36). There were much lower levels of separation on the upper surface, causing lower levels of drag and greater levels of lift enhancement when the airfoil was brought into the ground effect from the freestream.

Periodic Morphing

The aerodynamic characteristics of applying a periodically morphing trailing edge to a NACA6409 airfoil were investigated. Although DES has higher computational costs, periodic morphing has high flow details; therefore, DES is used for periodic morphing. The airfoil is morphed using the FishBAC method at a start location of 25% chord from the leading edge, varying the morphing frequency and trailing-edge displacement. The periodic morphing is investigated at 10% ground clearance at the 4° AoA. Initially, the simulation was run for 0.1 s with no morphing, where it was observed that the flow had fully settled. At 0.1 s, the morphing began, and the flow was allowed to settle before the time-averaged solution was recorded.

The baseline nonmorphed airfoil data had a time-averaged Cl of 1.157, Cd of 0.0152, and an aerodynamic efficiency of 76. The time-averaged lift and drag coefficients between 0.15 and 0.4 s (as mentioned in Methodology for periodic morphing) were shown in Figs. 37 and 38 for the periodically morphing airfoil. At a tip deflection of 0.1% at a morphing frequency of Strouhal number = 3.5 increased the lift by 2%; however, the drag also increased by 10%. The greater increase in drag caused the aerodynamic efficiency to reduce by 6.8. At a Strouhal number of 3.5 the lift and drag are higher than the baseline non-morphing airfoil for all trailing-edge displacements, which showed that by applying periodic morphing, the lift increased.

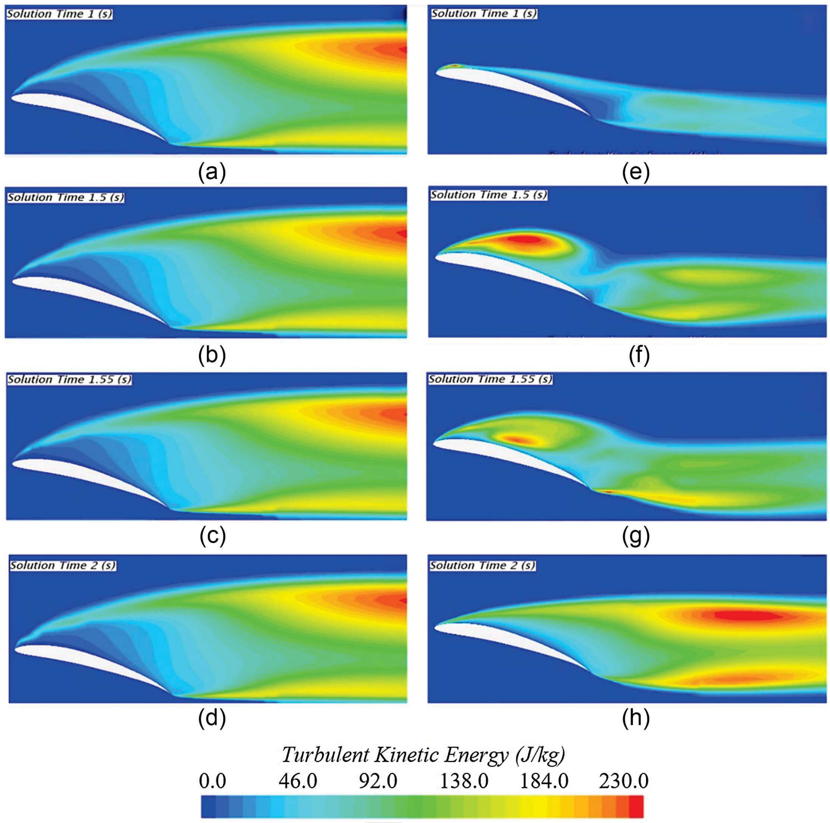

Fig. 35. NACA6409 TKE at 16° at (a)–(d) 10% ground clearance; and (e)–(h) and freestream.

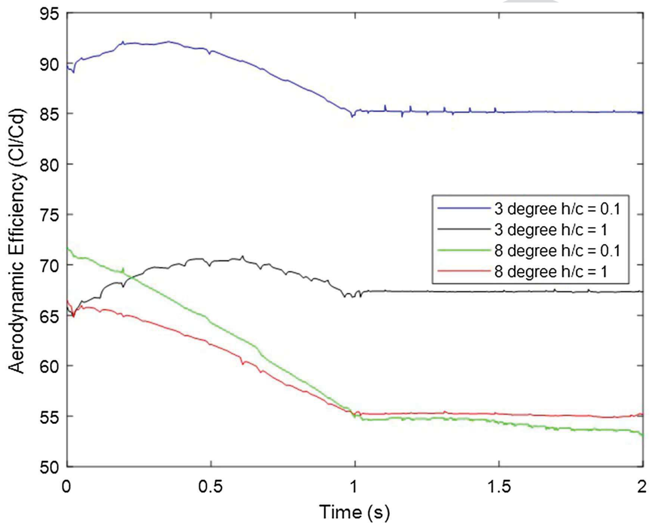

Fig. 36. Efficiency comparison between freestream and ground effect at low and high angles of attack.

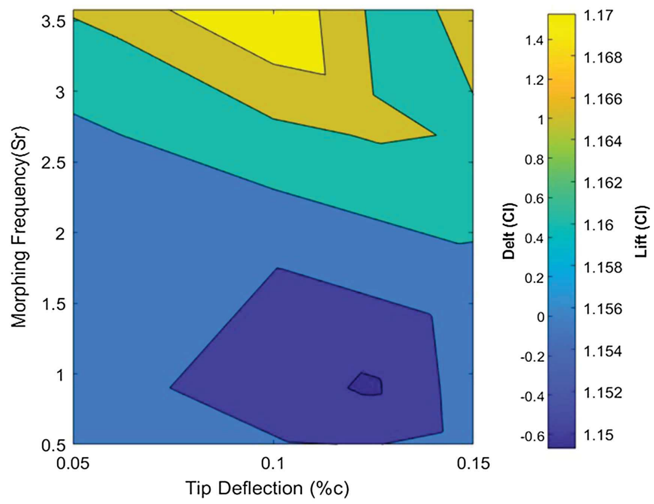

Fig. 37. Periodic morphing lift with a difference (delta) compared to non-morphing.

Reducing the morphing frequency from a Strouhal number of 3.5 showed that the lift and drag both reduced. At a Strouhal number of 2, the lift and drag are identical to the baseline airfoil, and reducing the morphing frequency further continued to reduce the drag and lift. At a Strouhal number of 0.9 at 0.05%, deflection drag reduced to 0.015 with a lift of 1.158. Increasing the trailing-edge displacement at a Strouhal number of 0.9 showed the lift and drag reduced but the drag reduced at a greater rate. This caused a peak efficiency of 80.5 (Fig. 39), an increase of 5.4% compared to the baseline airfoil.

Analyzing the peak efficiency morphing at a start location of 25%, Strouhal number of 0.9, and trailing-edge deflection of 0.125% showed that on the downwards deflection, the lift and drag

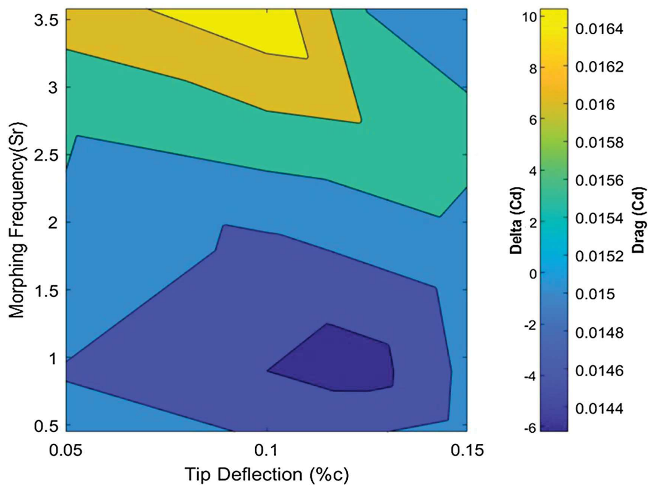

Fig. 38. Periodic morphing drag with a difference (delta) compared to non-morphing.

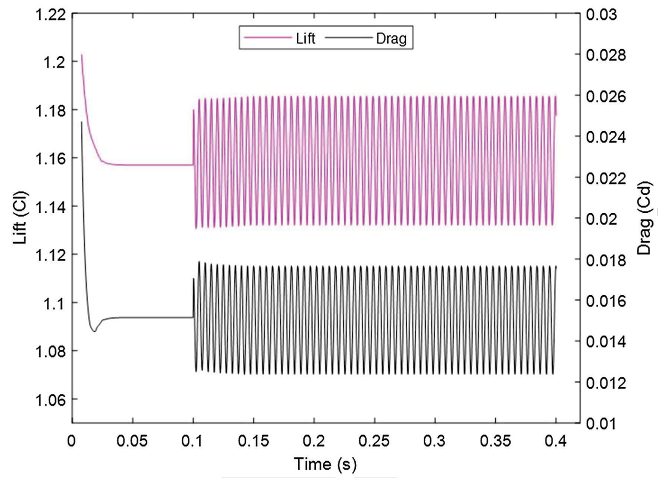

Fig. 40. Lift and drag raw data for 0.125% trailing-edge deflection at Strouhal number = 0.9 using DES.

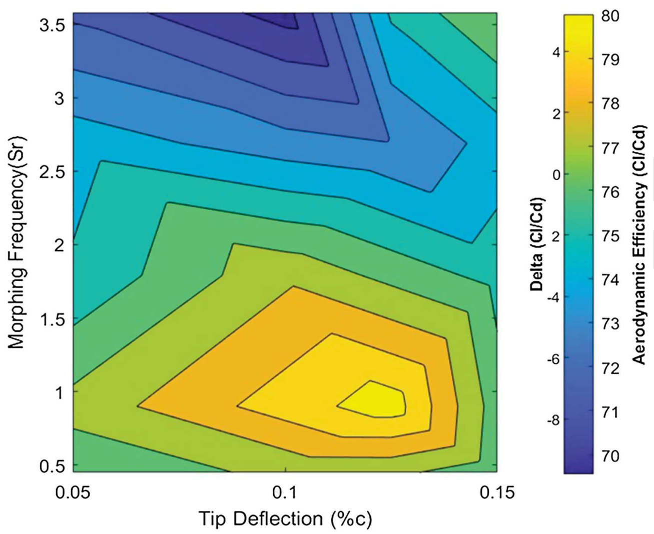

Fig. 39. Periodic morphing aerodynamic efficiency (Cl/Cd) with a difference (delta) compared to non-morphing.

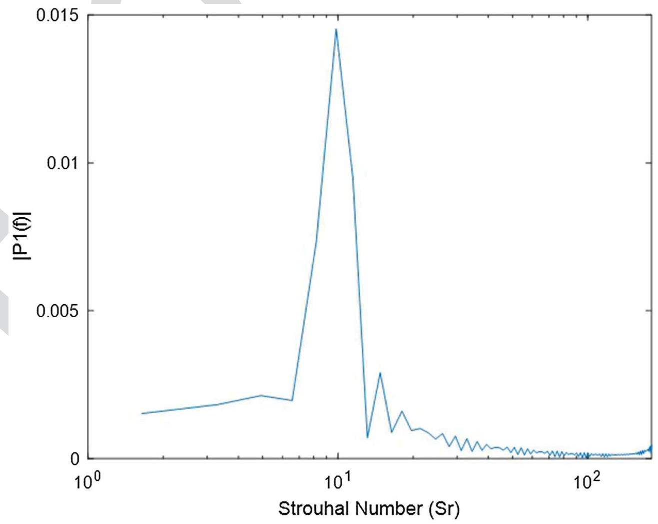

Fig. 41. Spectra plot for Strouhal number = 0.9 and 0.125% trailing-edge morphing airfoil in ground effect using DES for lift between 0.15 and 0.4 s.

increased and decreased on the upwards deflection (Fig. 40). The lift fluctuated by 3.8% around the mean lift, and the drag fluctuated by 30%.

The vorticity plot (Fig. 42) shows two distinct shear layers of fluid leaving the airfoil on the lower surface and on the upper surface above the separated flow region. The velocity of the flow leaving the trailing edge of both the upper and lower surfaces is equal, defined by the Kutta condition. Periodically morphing the airfoil caused these shear layers to slide over each other, causing instability in the wake after leaving the airfoil; the interaction between these two shear layers sliding over each other as the trailing edge was periodically morphed caused Kelvin–Helmholtz instability. Analyzing the spectra plot taken between 0.15 and 0.4 s for the lift (Fig. 41) showed a peak at a Strouhal number of 9.8. This value of the Strouhal number was similar to that reported by Jodin et al. (2017), who also saw Kelvin–Helmholtz instability for morphing an airfoil in freestream. The wake in (Fig. 42) is observed to oscillate in a standing wave characteristic periodically, and the total length of the wave is a quarter of that of a full sine wake before the wake dissipates into a negligible level of vorticity.

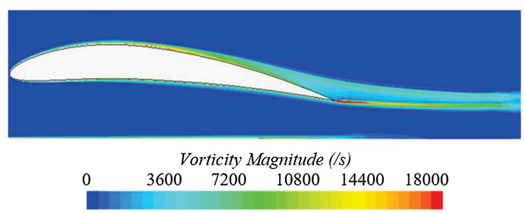

Fig. 42. Vorticity of NACA6409 periodically morphing in ground effect at Strouhal number = 0.9 and 0.125% trailing edge-deflection showing clear vorticity shear layers.

Conclusion

The performance of a trailing edge morphed NACA6409 airfoil in the ground effect is investigated using a two-dimensional RANS solver with a *k*-omega SST turbulence model. Three trailing-edge morphing lengths were tested beginning from the trailing edge at 10%, 15%, and 25% distances. With a fixed distance between the trailing edge and ground, starting the morphing later for 90% caused a greater distance between the airfoil lower surface and the ground upstream of the trailing edge, causing greater pressure on the morphed section, which resulted in higher lift compared to an earlier start location.

Varying the ground clearance of the morphed airfoil for the 3° AoA shows the enhancement in performance from the ground effect, with the highest gains when the wing is closest to the ground. The highest gains in lift were between $h/c = 0.2$ and $h/c = 0.1$ and the largest drag reduction between $h/c = 1$ and $h/c = 0.4$. The gains in lift varied between when brought into the ground effect from the freestream were between 10% and 17%; the larger gain is with the highest morphing deflection. There is a reduction in drag in the ground effect due to the proximity of the ground reducing the induced drag from the downwash. A key finding is a reduction in the distance between the ground and the trailing edge as the airfoil is morphed, causing further ground effect enhancement. Also, a later morphing start distance increased the area beneath the airfoil, which increased the lift and aerodynamic efficiency compared to an earlier morphing start location in the ground effect.

A dynamic morphing study is carried out morphing over a 1 s period to deflect the trailing edge 2.5% of the chord length; after the morphing period, the simulation is then left to run for the flow to settle. For dynamic morphing, the lift is almost identical to the static cases, while the drag is higher for the dynamic cases compared to the static morphing, which decreases the aerodynamic efficiency. Comparing the performance of dynamic freestream to dynamic in-ground showed that the ground effect efficiency is much higher than the freestream case for low AoAs. For the flow field, a highly oscillating vortex shedding wake is observed for the dynamic freestream above the 14° AoA causing high oscillations in lift and drag. In the ground effect at high AoAs, the proximity of the ground eliminated this vortex shedding, and the flow remained fully separated. In the ground effect, the NACA6409 stalled at 14° and freestream at 16°.

Applying periodic morphing to the NACA6409 airfoil in 10% ground effect at the 4° AoA using the FishBAC morphing method starting at 25% chord increased the aerodynamic efficiency from 76.4 to 80.5. This is an improvement in aerodynamic efficiency of 5.4%. The periodic morphing in the ground effect caused the upper and lower surfaces to interact and slide over each over, which caused a Kelvin–Helmholtz instability similar to (Jodin et al. 2017) in the freestream. Future work will extend the computational work to three dimensions, carry out wind tunnel tests, and implement the technology onto a UAV for flight tests.

Data Availability Statement

Some or all data, models, or codes that support the findings of this study are available from the corresponding author upon reasonable request.

Acknowledgments

This work was supported by the Engineering and Physical Sciences Research Council. The authors acknowledge the use of the IRIDIS High Performance Computing Facility, and associated support services at the University of Southampton, in the completion of this work.

Notation

The following symbols are used in this paper:

AoA = angle of attack;
Cd = drag coefficient;
CFL = Courant Friedrichs Lewy number;
Cl = lift coefficient;
c = chord length;
D = drag;
f = frequency;
GE = ground effect;
h = height above ground;
h/c = ground clearance to chord ratio;
L = lift;
LSD = lower surface distance;
l/d = aerodynamic efficiency;
Sr = Strouhal number;
TE = trailing edge;
TKE = turbulent kinetic energy;
t = time;
u = velocity;
Wte = trailing edge deflection to chord ratio;
Xs = morphing start location along chord;
x = distance along airfoil;
Yc = airfoil chord; and
Yt = airfoil thickness.

References

Abdessemed, C., A. Bouferrouk, and Y. Yao. 2021. “Aerodynamic and aeroacoustic analysis of a harmonically morphing airfoil using dynamic meshing.” *Acoustics* 3 (1): 177–199. https://doi.org/10.3390/acoustics3010013.

Abdessemed, C., A. Bouferrouk, and Y. Yao. 2022. “Effects of an unsteady morphing wing with seamless side-edge transition on aerodynamic performance.” *Energies* 15 (3): 1093. https://doi.org/10.3390/en15031093.

Abdessemed, C., Y. Yao, A. Bouferrouk, and P. Narayan. 2018. “Morphing airfoils analysis using dynamic meshing.” *Int. J. Numer. Methods Heat Fluid Flow* 28 (5): 1117–1133. https://doi.org/10.1108/HFF-06-2017-0261.

Abdessemed, C., Y. Yao, A. Bouferrouk, and P. Narayan. 2019. “Flow response to rapid morphing flap deflection.” In *Proc., 54th 3AF Int. Conf. on Applied Aerodynamics*. Paris: La Société Savante de l’Aéronautique et de l’Espace.

Abdessemed, C., Y. Yao, P. Narayan, and A. Bouferrouk. 2017. “Unsteady parametrisation of a morphing wing design for improved aerodynamic performance.” In *Proc., 52nd 3AF Int. Conf. on Applied Aerodynamics*. Paris: La Société Savante de l’Aéronautique et de l’Espace.

Coleman, H., and C. Members. 2009. *ASME V&V 20-2009 standard for verification and validation in computational fluid dynamics and heat transfer (V&V20 committee chair and principal author)*. New York: ASME.

Jodin, G., V. Motta, J. Scheller, E. Duhayon, C. Döll, J. F. Rouchon, and M. Braza. 2017. “Dynamics of a hybrid morphing wing with active open loop vibrating trailing edge by time-resolved PIV and force measures.” *J. Fluids Struct.* 74 (Oct): 263–290. https://doi.org/10.1016/j.jfluidstructs.2017.06.015.

Kan, Z., D. Li, J. Xiang, and C. Cheng. 2020. “Delaying stall of morphing wing by periodic trailing-edge deflection.” *Chin. J. Aeronaut.* 33 (2): 493–500. https://doi.org/10.1016/j.cja.2019.09.028.

Lee, T., and P. Gerontakos. 2004. "Investigation of flow over an oscillating airfoil." *J. Fluid Mech.* 512 (Aug): 313–341. https://doi.org/10.1017/S0022112004009851.

Lim, J. W., K. W. McAlister, and W. Johnson. 2009. "Hover performance correlation for Full-Scale and model-scale coaxial rotors." *J. Am. Helicopter Soc.* 54 (3): 32005. https://doi.org/10.4050/JAHS.54.032005.

Lissaman, P. B. S. 1983. "Low-Reynolds-number airfoils." *Ann. Rev. Fluid Mech.* 15 (1): 223–239. https://doi.org/10.1146/annurev.fl.15.010183.001255.

Menter, F. R. 1994. "Two-equation eddy-viscosity turbulence models for engineering applications." *AIAA J.* 32 (8): 1598–1605. https://doi.org/10.2514/3.12149.

Moore, N., P. A. Wilson, and A. J. Peters. 2002. *An investigation into wing in ground effect airfoil geometry*. RTO-MP-095. Neuilly-sur-Seine, France: North Atlantic Treaty Organisation (NATO), Research and Technology Organisation (RTO).

Narayanan, R. G. L., and O. C. Ibe. 2015. "Joint network for disaster relief and search and rescue network operations." In *Wireless public safety networks 1: Overview and challenges*, 163–193. Amsterdam, Netherlands: Elsevier.

Nirooei, M. 2018. "Aerodynamic and static stability characteristics of airfoils in extreme ground effect." *Proc. Inst. Mech. Eng., Part G: J. Aerosp. Eng.* 232 (6): 1134–1148. https://doi.org/10.1177/0954410017708212.

Ockfen, A. E., and K. I. Matveev. 2009. "Aerodynamic characteristics of NACA 4412 airfoil section with flap in extreme ground effect." *Int. J. Nav. Archit. Ocean Eng.* 1 (1): 1–12. https://doi.org/10.2478/IJNAOE-2013-0001.

Parameswaran, R., G. E. P. Box, W. G. Hunter, and J. S. Hunter. 1979. "Statistics for experimenters: An introduction to design, data analysis, and model building." *J. Marketing Res.* 16 (2): 291. https://doi.org/10.2307/3150696.

Qu, Q., X. Jia, W. Wang, P. Liu, and R. K. Agarwal. 2014. "Numerical study of the aerodynamics of a NACA 4412 airfoil in dynamic ground effect." *Aerosp. Sci. Technol.* 38 (Oct): 56–63. https://doi.org/10.1016/j.ast.2014.07.016.

Ravindra, K. 2018. "Do mesh still play a critical role in CFD." Accessed April 20, 2022. https://blog.gridpro.com/do-mesh-still-play-a-critical-role-in-cfd/.

Rozhdestvensky, K. V. 2006. "Wing-in-ground effect vehicles." *Prog. Aerosp. Sci.* 42 (3): 211–283. https://doi.org/10.1016/j.paerosci.2006.10.001.

Selig, M. S., J. F. Donovan, and D. B. Fraser. 1989. *Airfoils at low speeds*. Virginia Beach, VA: H. A. Stokely.

Siemens. 2016. "Siemens to acquire simulation software supplier CD-adapco." Accessed July 21, 2022. https://www.plm.automation.siemens.com/global/en/our-story/newsroom/siemens-press-release/43811.

Siemens. 2019. *User manual star CCM+ 854 14.04.013: Vol. 14.04.013 (p. transient term)*. Munich, Germany: Siemens.

Thakor, M., G. Kumar, D. Das, and A. De. 2020. "Investigation of asymmetrically pitching airfoil at high reduced frequency." *Phys. Fluids (1994)* 32 (5): 053607. https://doi.org/10.1063/5.0006659.

Wang, J. J., Y. C. Li, and K. S. Choi. 2008. "Gurney flap-lift enhancement, mechanisms and applications." *Prog. Aerosp. Sci.* 44 (1): 22–47. https://doi.org/10.1016/j.paerosci.2007.10.001.

Watkins, J., and A. Bouferrouk. 2022. "The effects of a morphed trailing-edge flap on the aeroacoustic and aerodynamic performance of a 30P30N aerofoil." *Acoustics* 4 (1): 248–267. https://doi.org/10.3390/acoustics4010015.

Weaver-Rosen, J. M., P. B. C. Leal, D. J. Hartl, and R. J. Malak. 2020. "Parametric optimisation for morphing structures design: Application to morphing wings adapting to changing flight conditions." *Struct. Multidiscip. Optim.* 62 (6): 2995–3007. https://doi.org/10.1007/s00158-020-02643-y.

Wilcox, D. C. 2008. "Formulation of the k-ω turbulence model revisited." *AIAA J.* 46 (11): 2823–2838. https://doi.org/10.2514/1.36541.

Winslow, J., H. Otsuka, B. Govindarajan, and I. Chopra. 2018. "Basic understanding of airfoil characteristics at low Reynolds numbers (104–105)." *J. Aircr.* 55 (3): 1050–1061. https://doi.org/10.2514/1.C034415.

Wolff, T., B. Ernst, and J. R. Seume. 2014. "Aerodynamic behavior of an airfoil with morphing trailing edge for wind turbine applications." *J. Phys.: Conf. Ser.* 524 (1): 012018. https://doi.org/10.1088/1742-6596/524/1/012018.

Woods, B. K. S., J. H. S. Fincham, and M. I. Friswell. 2014. *Aerodynamic modelling of the fish bone active camber morphing concept*. Bristol, UK: Royal Aeronautical Society Conference on Advanced Aero Concepts, Designs and Operations.

Woods, B. K. S., and M. I. Friswell. 2012. "Preliminary investigation of a fishbone active camber concept." In Vol. 45103 of *Smart materials, adaptive structures and intelligent systems*, 555–563. New York: ASME.

Xiang, J., K. Liu, D. Li, C. Cheng, and E. Sha. 2019. "Unsteady aerodynamic characteristics of a morphing wing." *Aircr. Eng. Aerosp. Technol.* 91 (1): 1–9. https://doi.org/10.1108/AEAT-04-2017-0101.

Yun, L., A. Bliault, and J. Doo. 2010. *WIG craft and Ekranoplan: Ground effect craft technology*. New York: Springer.

Zarim, M. A., A. Maimun, and M. R. Saad. 2016. "Wing in ground effect craft: A review of the state of current stability knowledge." In *Proc., Int. Conf. on Ocean Mechanical and Aerospace for Scientists and Engineer.* Kuala Lumpur, Malaysia: Universiti Pertahanan Nasional Malaysia.

Zhang, X., W. Toet, and J. Zerihan. 2006. *Ground effect aerodynamics of race cars*. Southampton, UK: Univ. of Southampton.

